ACS APPLIED MATERIALS & INTERFACES

www.acsami.org

Research Article

Ambient Cationic Activation-Radical Synergy Yields High-Performance Polymer Electrolytes

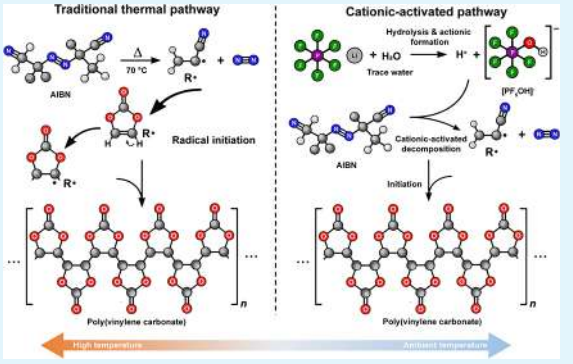
Zhong Xu, Weili Deng, and Weiqing Yang*

Cite This: ACS Appl. Mater. Interfaces 2026, 18, 35312−35323

Read Online

ACCESS | Metrics & More | Article Recommendations | Supporting Information

ABSTRACT: Conventional in situ thermal radical polymerization of electrolytes requires elevated temperatures and typically leads to complete monomer and Li-salt consumption, which severely limits ionic transport and results in an unstable solid-electrolyte interphase (SEI) for lithium metal batteries (LMBs). Here, we propose an ambient cationic activation-radical synergy strategy (CIP), in which PF_6^- derived Lewis acidic species selectively activate vinylene carbonate (VC) and trigger polymerization at room temperature through a cationic-induced pathway fundamentally distinct from the traditional thermal-initiated process (TIP). Combined theoretical calculations and in situ spectroscopic analyses indicate that PF_6^- decomposition precedes polymer growth and lowers the activation barrier, enabling controlled polymerization while preserving a fraction of electrochemically active monomers. The resulting gel polymer electrolyte (GPE) exhibits accelerated ionic transport kinetics with an elevated transference number of 0.78 and an ionic conductivity of 6.49×10^{-3} S cm^{-1}. When applied in LMBs, this electrolyte promotes the formation of a dense, inorganic-rich, and dynamically reinforced SEI, enabling stable lithium plating/stripping over 2000 h, sustained cycling over 1200 cycles at 0.5 C, and excellent rate capability up to 10 C, demonstrating its promise for high-performance LMBs.



KEYWORDS: *cationic activation-radical synergy, gel polymer electrolyte, in-situ polymerization, lithium-ion transport kinetics, solid-electrolyte interphase*

1. INTRODUCTION

Polymer electrolytes are pivotal enabling materials for advanced LMBs, offering intrinsic safety, mechanical flexibility, and the capability to regulate interfacial chemistry through molecular-level design.[1−5] However, achieving simultaneously high ionic conductivity, an elevated Li^+ transference number, and robust interfacial stability in polymer electrolytes remains a formidable challenge.[6−8] To address these issues, in situ polymerization electrolytes have attracted growing interest, as they enable conformal electrolyte formation and dynamic interphase regulation directly within the cells.[9−12]

Despite their promise, conventional in situ polymerization of liquid electrolytes is predominantly reliant on thermal radical initiation, which typically requires elevated temperatures and leads to uncontrolled consumption of monomers and lithium salts.[13−15] Such indiscriminate polymerization generates highly cross-linked and rigid polymer networks, severely restricting segmental motion and ion mobility. Furthermore, the substantial loss of electrochemically active species fundamentally limits the attainable ionic conductivity and Li^+ transference number, thereby constraining the rate capability and long-term stability of LMBs.[16] In commercial liquid electrolytes, lithium hexafluorophosphate ($LiPF_6$) serves as the ubiquitous salt, which is conventionally regarded as chemically fragile due to its tendency to generate Lewis acidic species (PF_5) through hydrolysis, particularly under trace moisture or high-voltage conditions.[17−21] While traditionally considered a detrimental side reaction, recent work by Liu demonstrated that trace moisture-triggered PF_6^- hydrolysis can generate proton-containing intermediates (e.g., $H^+(PF_5OH)^-$) that initiate cationic polymerization at room temperature.[22] This suggests that the intrinsic reactivity of $LiPF_6$, rather than being purely undesirable, could be harnessed to drive controlled polymerization under mild conditions—an opportunity that remains largely unexplored.

Herein, we propose an ambient cationic activation-radical synergy strategy that redefines the role of PF_6^- anions in gel polymer electrolyte systems. Building on the moisture-initiated cationic polymerization concept, PF_6^- -derived Lewis acidic species are proposed to interact with Azobis(isobutyronitrile) (AIBN) and vinylene carbonate (VC), triggering polymer-

Received: March 24, 2026
Revised: June 4, 2026
Accepted: June 14, 2026
Published: June 17, 2026



ACS Publications

© 2026 American Chemical Society

Downloaded from pubs.acs.org/aamick/article-pdf/18/25/35312/6511266/acsami.6c06006.pdf by SOUTHWEST JIAOTONG UNIV user on 07 November 2026

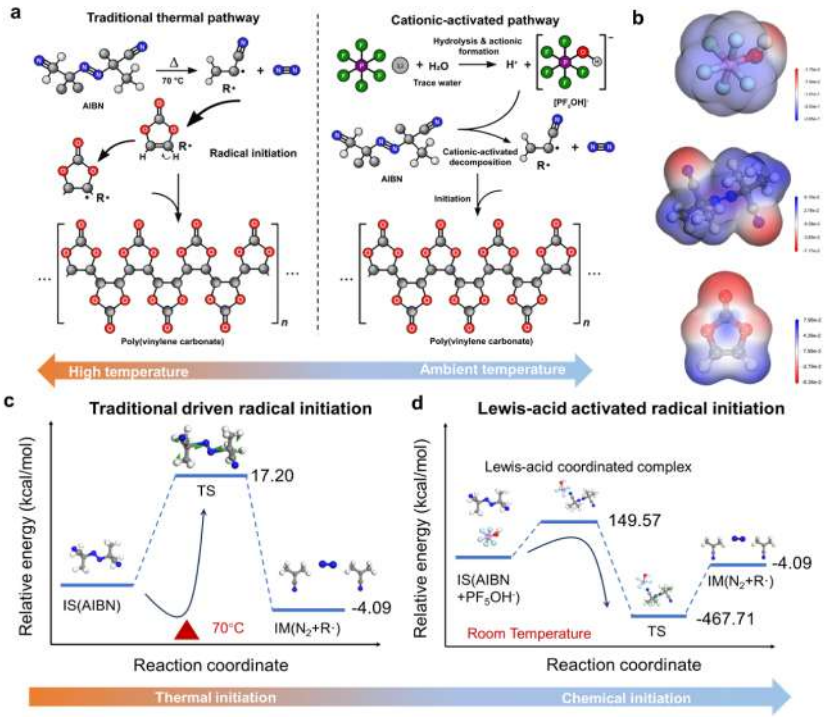


Figure 1. Design of the ambient cationic activation-radical synergy strategy for polymer electrolyte. a. Schematic illustration comparing the traditional thermal pathway and cationic-activated pathway. b. Electrostatic potential (ESP) maps of PF6-derived Lewis acidic species, AIBN and VC. Calculation of reaction free-energy profiles for VC polymerization via c. thermal radical initiation and d. PF6-mediated cationic activation pathways.

ization at room temperature through a cationic-induced pathway synergistically coupled with radical propagation. Crucially, this anion-involved polymerization contributes to the retention of PF_6^--derived species within the gel polymer matrix, suppressing anion mobility and reshaping the population of mobile charge carriers. As a consequence, the resulting gel polymer electrolyte achieves a high ionic conductivity (6.49×10^{-3} S cm^{-1}) and a markedly enhanced Li^+ transference number (0.78). When applied in LMBs, this GPE facilitates the formation of a dense, inorganic-rich, and dynamically reinforced SEI layer, enabling stable high-rate capacity of 68 mAh g^{-1} @10C, prolonged lifespan exceeding 2000 h @0.5 mA cm^{-2}, and a high average Coulombic efficiency of 99.98%. Overall, this cationic activation-radical synergy strategy transforms the intrinsic instability of salt anions into a driving force for GPE synthesis, opening a new avenue for rationally designing gel polymer electrolytes with decoupled ion conduction and enhanced Li^+ transport, offering broad implications for high-energy-density LMBs.

2. RESULTS AND DISCUSSION

2.1. Design Principle of Cationic-Activated Pathway

Conventional in situ thermal radical polymerization of VC monomers typically requires elevated temperatures or UV irradiation to activate radical initiators (e.g., AIBN), inevitably driving complete monomer consumption and anion involvement in the polymer matrix.[23,24] Such uncontrolled polymerization not only suppresses ionic mobility but also results in sluggish Li^+ transport dominated by coupled anion migration.[25] To overcome these intrinsic limitations, we propose an ambient cationic-activated pathway that harnesses rather than avoids the latent reactivity of of $LiPF_6$ (Figure 1). As illustrated in Figure 1a, the proposed pathway draws on the moisture-initiated cationic polymerization, where trace H_2O is suggested to react with PF_6^- to generate Lewis acidic intermediates (e.g., PF_5 and related proton-containing species), which serve as catalytic triggers. These electrophilic intermediates are proposed to selectively interact with the electron-rich sites of AIBN and VC, forming transient cationic activation complexes that lower the activation energy for room-temperature polymerization. Importantly, this mechanism is accompanied by the retention of PF_6^--derived fluorophosphate species within the growing gel polymer framework, contributing to anion immobilization and shifting the charge carrier population toward Li^+ dominance.[26]

Density functional theory calculations provide molecular-level insights into this cationic activation mechanism. Electrostatic potential (ESP) maps effectively reveal pronounced electrophilic regions on PF_6^- derived Lewis acidic species (Figure 1b). Upon coordination, these species induce strong polarization of the C=C bond in VC and the azo bond in AIBN. This creates a Lewis-acid-coordinated transition state that stabilizes the incipient cationic character during bond cleavage, facilitating a chemically assisted activation pathway unattainable through purely thermal means. Consequently, the polymerization follows a distinct paradigm—an anion-triggered cationic initiation synergistically coupled with radical propagation.[27] This mechanistic switch is further substantiated by reaction free-energy profiles (Figure 1c and 1d). The formation of PF_6^- eactive Lewis acidic species significantly lowers the kinetic barrier for bond dissociation compared to the thermal route, enabling spontaneous polymerization under ambient conditions. Importantly, this moderated activation energy prevents the runaway consumption of VC and lithium salts often seen in thermal methods, ensuring that a sufficient

https://doi.org/10.1021/acsami.6c06006
ACS Appl. Mater. Interfaces 2026, 18, 35312−35323

Downloaded from pubs.acs.org/aamick/article-pdf/18/25/35312/6511266/acsami.6c06006.pdf by SOUTHWEST JIAOTONG UNIV user on 07 November 2026

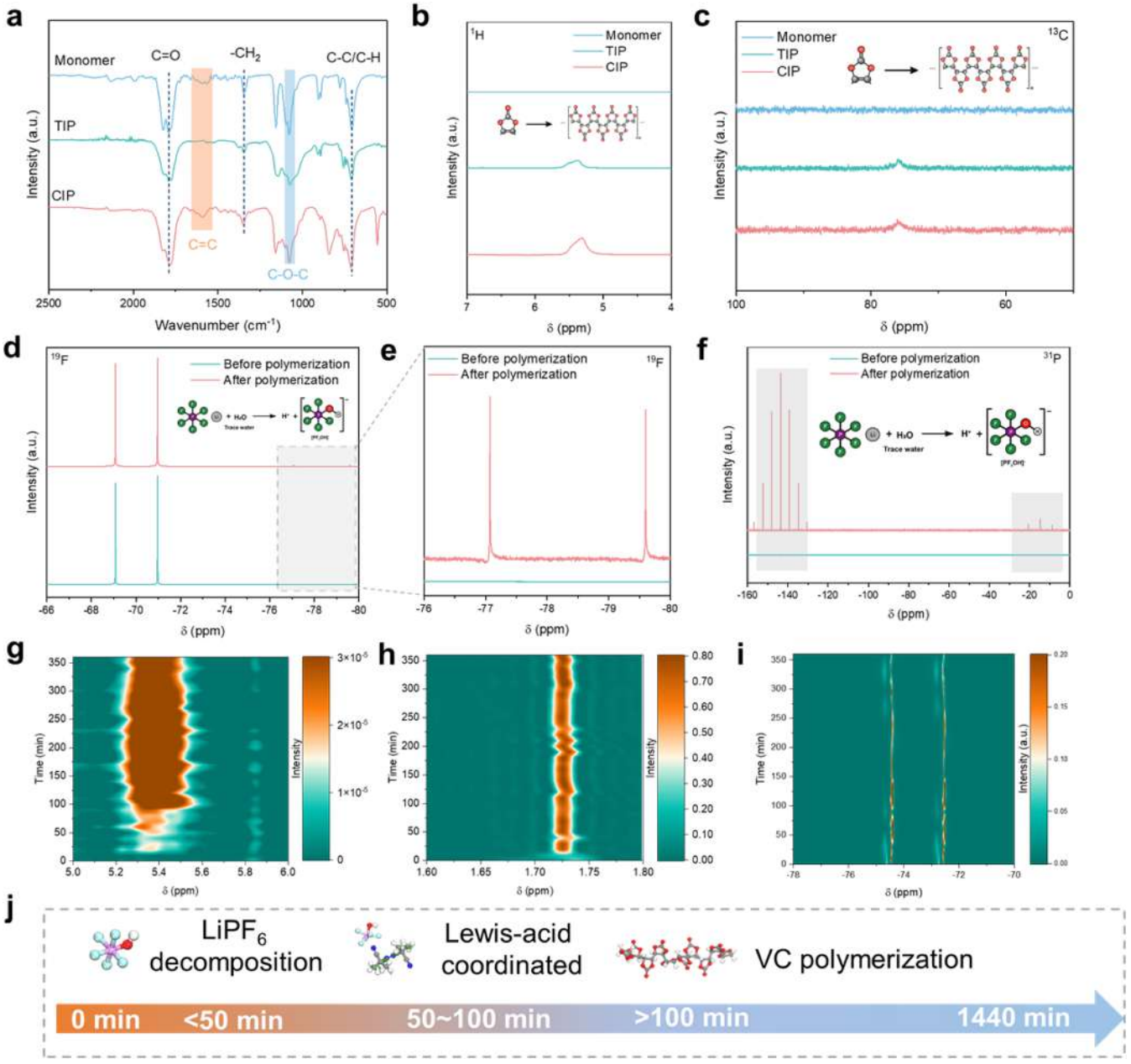


Figure 2. Characterization of chemical evolution of the electrolyte during polymerization. a. Fourier transform infrared spectra of monomer and polymer electrolyte during TIP and CIP polymerization. b. 1H nuclear magnetic resonance spectra of monomer and polymer electrolyte during TIP and CIP polymerization. c. ^{13}C NMR spectra of monomer and polymer electrolyte during TIP and CIP polymerization. d. ^{19}F NMR spectra of polymer electrolyte before and after CIP polymerization, and e. locally enlarged views. f. ^{31}P NMR spectra of polymer electrolyte before and after CIP polymerization. In-situ g. ^{1}H, h. ^{7}Li, i. ^{19}F NMR spectra at the early stage of the polymerization. j. Schematic illustration of the detailed formation process of the polymer electrolyte via the CIP, highlighting PF6-derived Lewis acidic species-induced activation, room-temperature polymerization, and the resulting interconnected polymer network.

fraction of electrochemically active species is retained for ion conduction. Ultimately, by incorporating PF_6^- derived moieties into localized coordination environments, this strategy reconstructs the ion-transport landscape: anion mobility is restricted, while cation-dominated Li^+ conduction is promoted. This establishes a direct link between chemically programmed polymerization and enhanced transport kinetics, offering a rational framework for high-performance polymer electrolytes.

2.2. Chemical Evolution of the Electrolyte during Cationic-Activated Polymerization

While the above theoretical analyses establish the energetic feasibility and molecular origin of the PF_6^- mediated cationic activation-radical synergy, direct experimental evidence is needed to assess whether the proposed anion-involved pathway operates under practical conditions. In particular, probing the early stage participation of PF_6^--derived species and the temporal relationship between salt decomposition and VC polymerization is important for evaluating the mechanistic distinction from conventional thermal radical processes. To

https://doi.org/10.1021/acsami.6c06006
ACS Appl. Mater. Interfaces 2026, 18, 35312−35323

Downloaded from pubs.acs.org/aamick/article-pdf/18/25/35312/6511266/acsami.6c06006.pdf by SOUTHWEST JIAOTONG UNIV user on 07 November 2026

this end, we employ a combination of ex-situ structural characterization and in-situ spectroscopic techniques to track the chemical evolution of the electrolyte during polymerization. As shown in Figure 2a, Fourier transform infrared (FTIR) spectra reveal distinct chemical evolution during both TIP and CIP polymerization processes. Notably, the C═O stretching vibration of VC exhibits a pronounced redshift after polymerization, which is significantly more evident in the CIP electrolyte. This redshift originates from the involvement of PF_6^- derived Lewis acidic species that interact with the carbonate groups, inducing electron density redistribution and strengthening the coordination between C═O moieties and Li^+ ions.[28] Such Lewis acid-mediated activation effectively weakens the C═O bond strength, giving rise to the observed shift toward lower wavenumbers.[29] Meanwhile, the characteristic C═C stretching band of VC completely vanishes in the TIP electrolyte, indicating exhaustive monomer consumption under thermal radical initiation. In contrast, a discernible C═C signal persists in the CIP electrolyte, confirming that a fraction of VC monomers is retained within the polymer matrix as a result of the moderated, cationic-activated polymerization pathway. The coexistence of polymerized segments and mobile monomers is expected to enhance segmental dynamics and facilitate ion transport.[30−32]

Consistent with the FTIR results, combined ^1H and ^{13}C NMR analyses (Figure 2b, c, and Figures S1−2) provide direct molecular-level evidence for VC polymerization in both TIP and CIP electrolytes. In the ^1H NMR spectra, the vinyl proton resonance of VC at ∼5.4 ppm, which corresponds to aliphatic C−H protons of the poly(vinylene carbonate) backbone, emerges upon polymerization.[33] The ^{13}C NMR spectra show the concomitant disappearance of the vinyl carbon signal at ∼78 ppm, together with the emergence of new carbonate-related carbon environments. These features confirm the formation of poly(vinylene carbonate) (PVC) through both polymerization routes. Notably, in the CIP electrolyte, residual sharp proton signals and relatively narrower resonances remain observable, indicating the coexistence of PVC chains with a fraction of unreacted VC monomers and solvent molecules. This spectral signature reflects a moderated, cation-activated polymerization pathway in CIP GPE, which preserves molecular mobility and dynamic species within the electrolyte matrix. To directly probe the involvement of PF_6^- anions during CIP polymerization, combined ^{19}F and ^{31}P NMR analyses were performed before and after polymerization. As shown in Figure 2d−f, both fluorine and phosphorus spectra undergo pronounced evolution upon polymerization, manifested by peak broadening, intensity redistribution, and the emergence of new resonances. These features indicate the decomposition of $LiPF_6$ and the formation of new fluorine-containing species, while the concomitant appearance of additional ^{31}P signals directly evidences the generation of new phosphorus chemical environments.[34] To further support this interpretation, XPS analysis of the polymerized electrolyte after the CIP process was conducted (Figure S3). The O 1s and C 1s spectra confirm the formation of carbonate/polycarbonate species, while the P 2p and F 1s spectra reveal residual PF_6^- together with fluorophosphate and LiF species, indicating partial transformation of $LiPF_6$ during polymerization. The Li 1s and N 1s spectra further verify the formation of lithium-containing interphase species and AIBN-derived nitrile species. These observations are consistent with the NMR results and support the involvement of PF_6^--derived Lewis acidic intermediates in the polymerization process. Collectively, these results provide direct spectroscopic proof that $LiPF_6$ undergoes partial decomposition and actively participates in the CIP polymerization process, rather than serving as an inert supporting salt. To further clarify the indispensable role of $LiPF_6$ in triggering the polymerization, a series of experiments were conducted under identical resting conditions. As shown in Figure S4, binary combinations of VC, $LiPF_6$, and AIBN were systematically examined. Notably, polymerization accompanied by macroscopic solidification was observed exclusively in the ternary "VC+$LiPF_6$+AIBN" system, whereas other mixtures remained in a liquid state, indicating that none of the individual components or their pairwise interactions is sufficient to initiate polymerization at room temperature. Meanwhile, the role of the lithium salt chemistry was probed by replacing $LiPF_6$ with alternative salts, including LiTFSI and $LiClO_4$. Despite the presence of VC and AIBN, no polymerization or solidification was observed in these systems under identical conditions (Figure S5). In sharp contrast, only electrolytes containing $LiPF_6$ underwent spontaneous polymerization at ambient temperature, unambiguously demonstrating that the PF_6^- anion plays a unique and irreplaceable role in activating the polymerization pathway. In Movie S2, we use butylated hydroxytoluene (BHT) to confirm the decomposition of AIBN and free-radical generation during the polymerization process. When the radical inhibitor BHT is introduced, the gelation process is completely suppressed, indicating that free-radical reactions play a critical role in the polymerization process.

To capture the early-stage reaction dynamics, in situ NMR measurements were performed during the initial polymerization process. As shown in Figure 2g, the in situ ^1H NMR spectra reveal that the characteristic proton resonance associated with PVC formation at ∼5.4 ppm emerges only after approximately 100 min, indicating that macroscopic polymer growth occurs at a relatively later stage. In sharp contrast, pronounced spectral evolution is already observed at much earlier times (<50 min) in both the ^7Li (Figure 2h) and ^{19}F NMR spectra (Figure 2i), including line-shape distortion and signal broadening. These early changes in the Li and F spectra directly evidence the preferential decomposition of $LiPF_6$ and the rapid reconfiguration of Li^+ coordination and PF_6^- species prior to polymer chain formation. Such temporal decoupling unambiguously demonstrates that $LiPF_6$ decomposition precedes and catalytically induces AIBN activation and subsequent radical polymerization of VC, rather than polymerization occurring through a concerted or purely thermal pathway.[35]

A continuous record of the room-temperature polymerization process is provided in Figure S6 and Movie S1, capturing the gradual evolution of the electrolyte from a low-viscosity liquid to a fully gelled state. The system undergoes a progressive viscosity increase and reaches complete gelation after approximately 21 h, confirming the spontaneous and self-sustained nature of the CIP polymerization under ambient conditions. Representative photographs corroborate the formation of a homogeneous polymer network. The high optical transparency shown in Figure S7 indicates uniform polymerization without macroscopic phase separation, whereas Figure S8 confirms the successful in situ formation of the polymer electrolyte within the cell, highlighting its practical applicability. The surface and cross-sectional morphologies of the polymer electrolyte are shown in Figures S9−10. The

Downloaded from pubs.acs.org/aamick/article-pdf/18/25/35312/6511266/acsami.6c06006.pdf by SOUTHWEST JIAOTONG UNIV user on 07 November 2026

https://doi.org/10.1021/acsami.6c06006
ACS Appl. Mater. Interfaces 2026, 18, 35312−35323

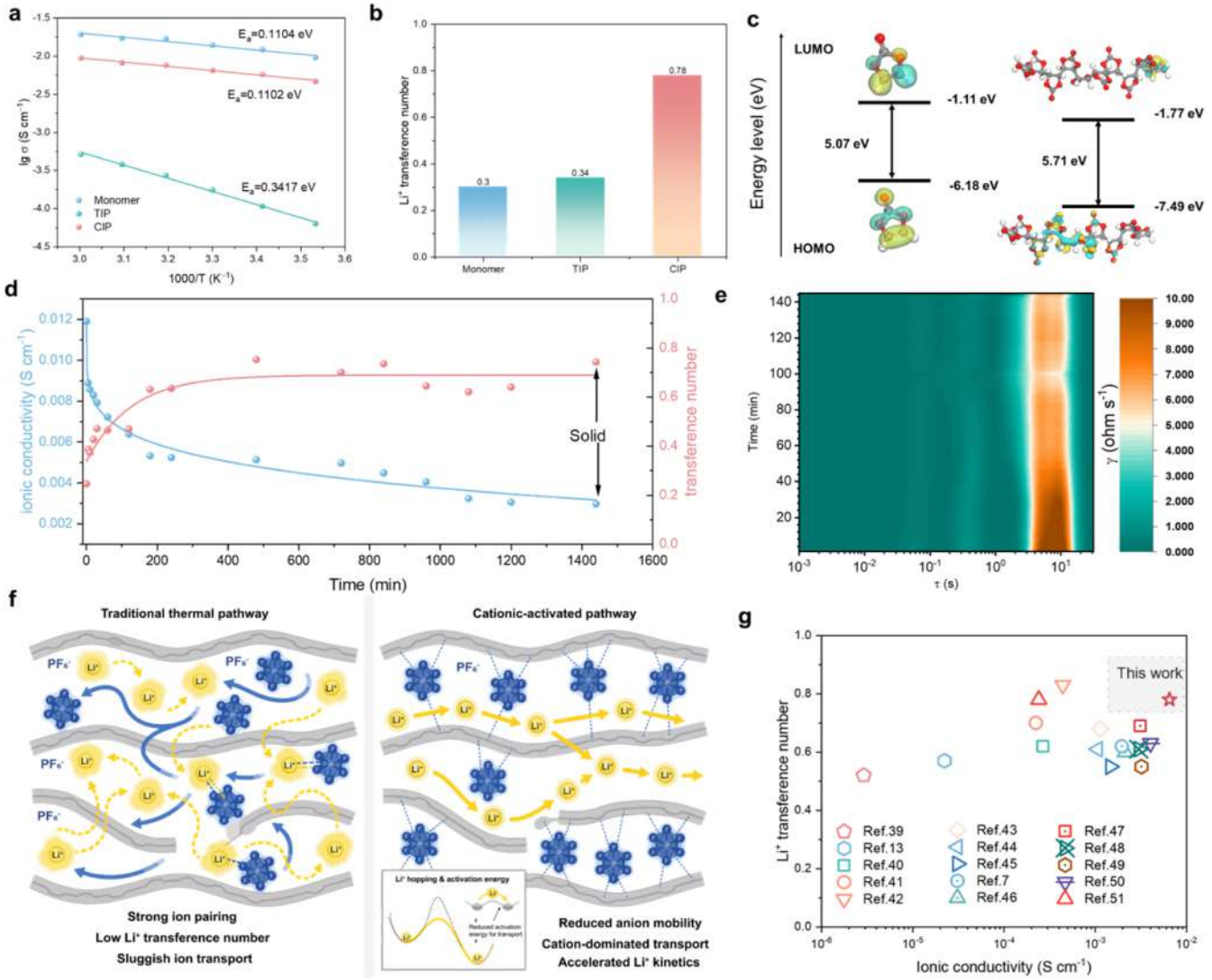


Figure 3. Anion confinement Li^+ transport kinetics in polymer electrolyte. a. Arrhenius plots of ionic conductivity for the VC monomer, TIP, and CIP electrolyte, together with the corresponding activation energies extracted from linear fitting. b. Li^+ transference numbers of the VC monomer, TIP, and CIP electrolytes. c. Calculated HOMO and LUMO energy levels of VC monomer and PVC. d. Evolution of ionic conductivity and Li^+ transference number during the CIP polymerization process, revealing the decoupled regulation of σ and t+ as polymerization proceeds. e. In-situ distribution of relaxation times (DRT) spectra recorded at the early stage of CIP polymerization, evidencing the dynamic reconstruction of ion-transport processes. f. Schematic illustration of Li^+ transport pathways in polymer electrolytes obtained via TIP and CIP. g. Performance comparison of σ and t+ between this work and recently reported polymer electrolytes within the past year.

surface is composed of uniformly distributed particulate features with characteristic sizes of ~2 μm, whereas the cross-section exhibits a dense and continuous morphology, consistent with the formation of an interconnected polymer network. In addition, X-ray diffraction (XRD) patterns of polymer electrolytes obtained via both TIP and CIP routes in Figure S11 display a single broad diffraction halo without discernible crystalline reflections, suggesting an amorphous or weakly semicrystalline structure in both cases. Such disordered polymer frameworks are widely recognized as favorable for ion transport in polymer electrolytes.[36] The TG results of CIP and TIP electrolytes (Figure S12) show similar overall weight-loss behaviors, indicating comparable polymer conversion levels. Both samples undergo initial volatilization of residual components followed by decomposition of the polymerized framework. Compared with TIP, CIP exhibits a slightly delayed decomposition onset and higher residual mass, suggesting enhanced thermal stability associated with a more robust polymer network.

2.3. Anion Confinement-Enabled Li^+ Transport Kinetics in Polymer Electrolytes

Taken together, these characterization results demonstrate that the CIP process yields a homogeneous, amorphous gel polymer electrolyte (GPE) while selectively immobilizing PF_6^- derived species. This unique chemical and structural configuration is expected to fundamentally alter the ion-transport landscape, motivating a detailed investigation of Li^+ transport kinetics and transference behavior. The temperature-dependent ionic conductivities of the VC monomer electrolyte, TIP, and CIP polymer electrolytes are shown in Figure 3a and Figure S13. The conductivity of the TIP electrolyte decreases markedly to 1.76×10^{-4} S cm^{-1} after complete polymerization, reflecting restricted ion mobility in the densely cross-linked polymer matrix. In contrast, the CIP electrolyte maintains a

https://doi.org/10.1021/acsami.6c06006
ACS Appl. Mater. Interfaces 2026, 18, 35312−35323

Downloaded from pubs.acs.org/aamick/article-pdf/18/25/35312/6511266/acsami.6c06006.pdf by SOUTHWEST JIAOTONG UNIV user on 07 November 2026

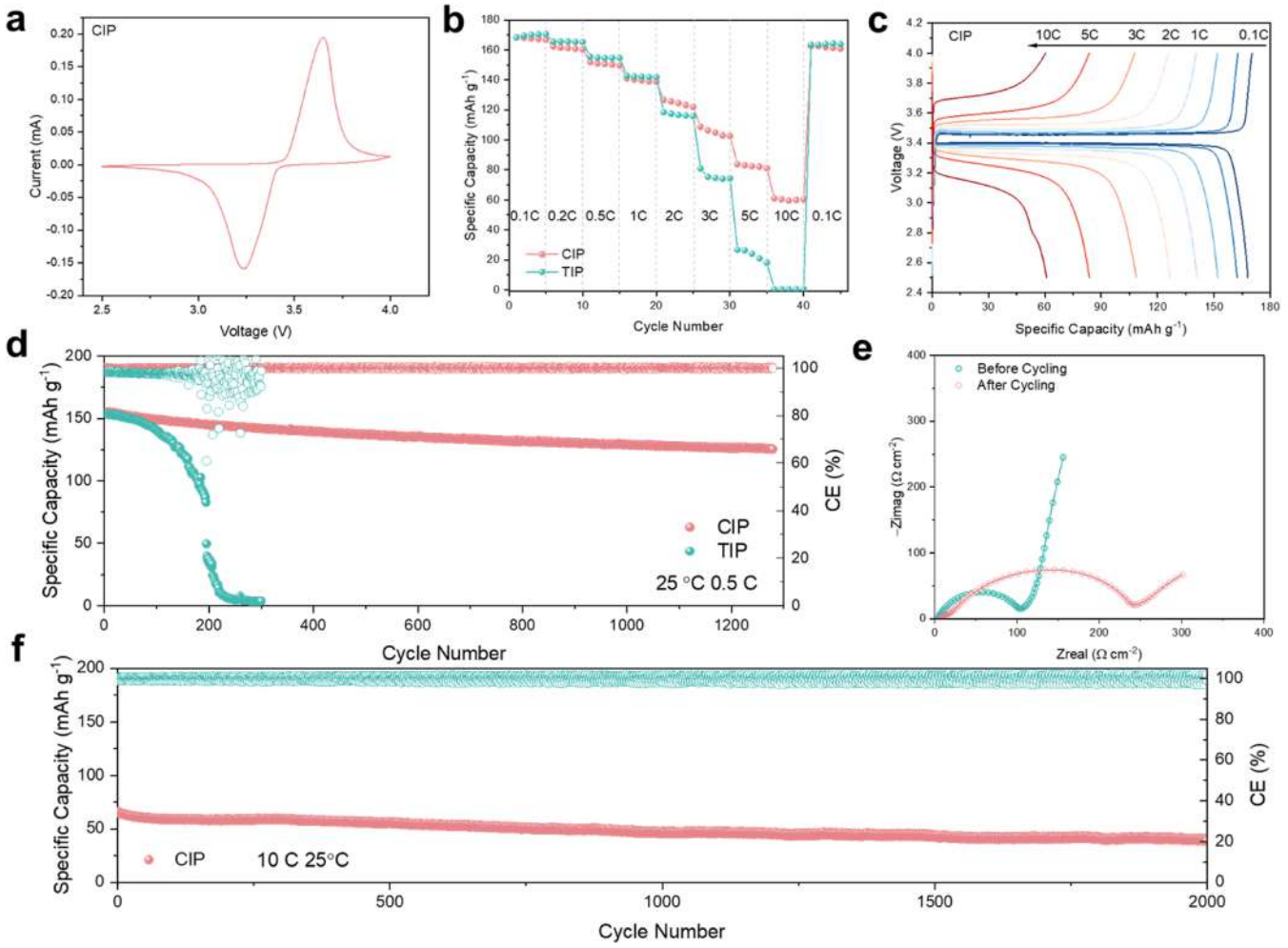


Figure 4. Electrochemical performance of LMBs enabled by the polymer electrolyte. a. Cyclic voltammetry profiles of LMBs employing the CIP electrolyte. b. Rate performance of LMBs based on TIP and CIP electrolytes measured from 0.1 to 10 C. c. Representative charge/discharge voltage profiles of the CIP-based LMBs from 0.1 to 10 C. d. Long-term cycling performance and corresponding Coulombic efficiency of LMBs at 0.5 C. e. Electrochemical impedance spectra of the CIP-based battery measured before and after prolonged cycling. f. High-rate cycling performance and corresponding Coulombic efficiency of the CIP-based battery operated at 10 C.

substantially higher ionic conductivity of 6.49×10^{-3} S cm^{-1} at room temperature, despite the formation of a polymer network. Linear fitting of the Arrhenius plots yields apparent activation energies of 0.1104, 0.1102, and 0.3417 eV for the VC monomer, TIP, and CIP electrolytes, respectively. Notably, the CIP electrolyte exhibits a significantly lower activation energy than the TIP counterpart, indicating facilitated ion hopping and reduced transport barriers enabled by the cationic-activated polymerization pathway.[37]

Figure 3b and Figures S14−15 compare the Li^+ transference numbers (t^+) of the three electrolytes. The VC monomer electrolyte shows a relatively low t^+ of 0.30, characteristic of conventional liquid electrolytes dominated by mixed anion−cation transport. Upon thermal radical polymerization, the TIP electrolyte exhibits only a marginal increase to 0.34, owing to the simultaneous immobilization of both cations and anions within the polymer matrix. Strikingly, the CIP electrolyte delivers a substantially elevated t^+ of 0.78, approaching cation-dominated ion transport. This pronounced enhancement directly reflects the preferential confinement and chemical immobilization of PF_6^- derived species during CIP polymerization, leaving Li^+ as the primary mobile charge carrier in the electrolyte. To elucidate the electrochemical stable window of the electrolyte, density functional theory calculations were performed to analyze the frontier molecular orbitals of VC and PVC (Figure 3c). The VC monomer exhibits a HOMO−LUMO gap of 5.07 eV, whereas polymerization to PVC results in a modified electronic structure with a reduced gap of 5.71 eV. Moreover, the linear sweep voltammetry curve also indicates that the CIP electrolyte exhibits the highest electrochemical stable window, as seen in Figure S16. This evolution in electronic structure suggests enhanced electronic delocalization and polarizability in the polymeric state, which facilitates stronger interactions with Lewis-acidic PF_6^- derived species and promotes electrochemical stability at higher voltages.[38]

Figure 3d tracks the evolution of ionic conductivity and Li^+ transference number during the CIP polymerization process. At the initial stage, the electrolyte exhibits high conductivity but a relatively low t^+, resembling liquid-like transport behavior. As polymerization proceeds, the ionic conductivity gradually decreases from 1.2×10^{-2} to 6.49×10^{-3} S cm^{-1}, while the t^+ increases monotonically from 0.25 to 0.78. This opposite evolution of σ and t^+ clearly demonstrates the decoupling of ionic conductivity and Li^+ transport selectivity in the CIP electrolyte, in sharp contrast to conventional polymer

https://doi.org/10.1021/acsami.6c06006
ACS Appl. Mater. Interfaces 2026, 18, 35312−35323

Downloaded from pubs.acs.org/aamick/article-pdf/18/25/35312/6511266/acsami.6c06006.pdf by SOUTHWEST JIAOTONG UNIV user on 07 November 2026

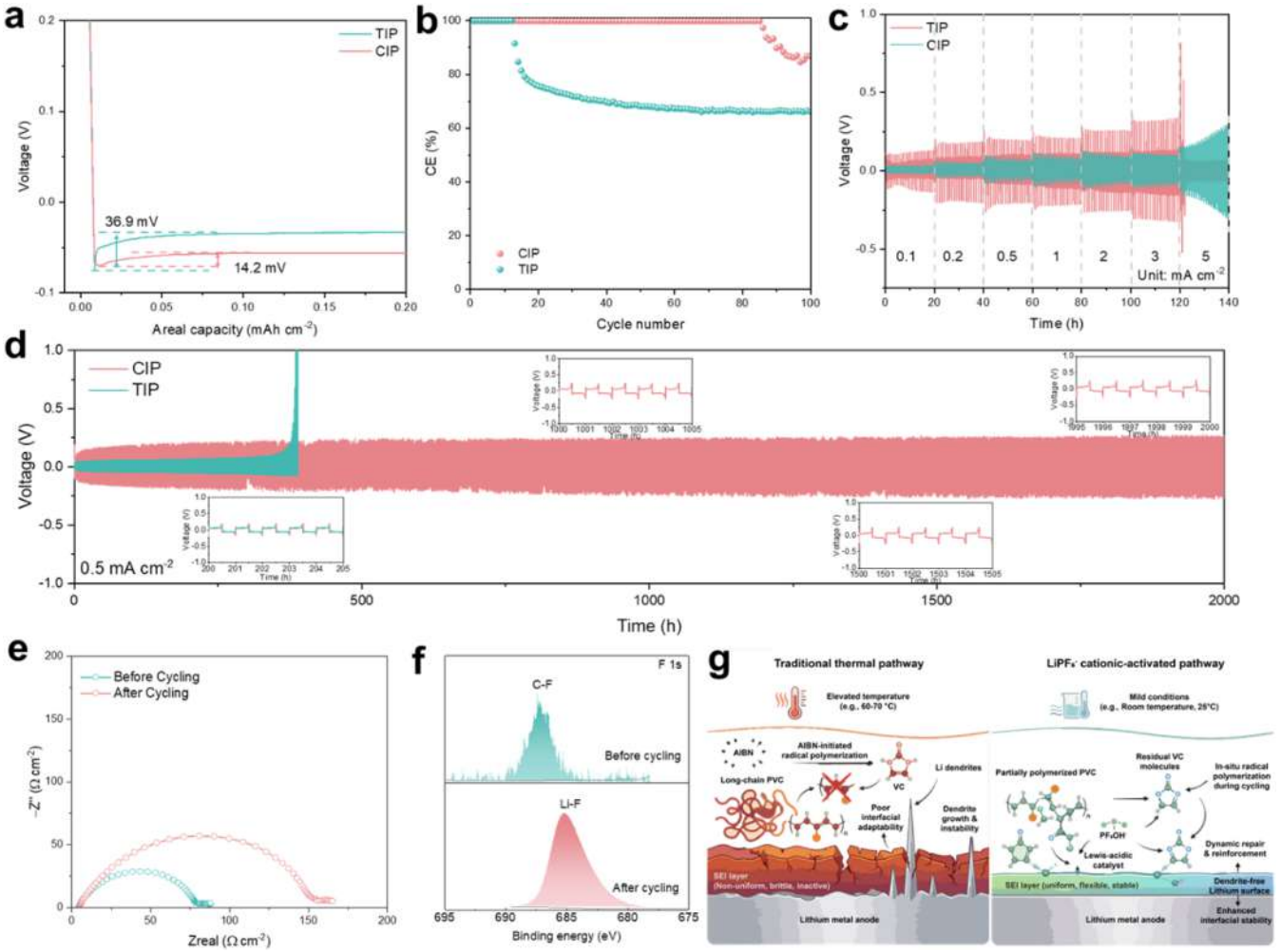


Figure 5. Interfacial stabilization of lithium metal anodes enabled by the CIP electrolyte. a. Comparison of lithium nucleation overpotentials for Li deposition in electrolytes prepared via TIP and CIP. b. Coulombic efficiency of Li−Cu cells cycled with TIP and CIP electrolytes. c. Critical current density of Li symmetric cells employing TIP and CIP electrolytes. d. Long-term cycling performance of Li symmetric cells at 0.5 mA cm^{-2} using TIP and CIP electrolytes. e. Electrochemical impedance spectra of Li symmetric cells with the CIP electrolyte before and after prolonged cycling, revealing the evolution of interfacial resistance. f. F 1s X-ray photoelectron spectroscopy spectra of CIP electrolyte before and after long-term cycling. g. Schematic illustration comparing SEI formation and interfacial evolution in TIP and CIP electrolytes.

electrolytes, where both parameters typically deteriorate simultaneously. To further probe the dynamic reconstruction of ion-transport pathways, in situ distribution of relaxation times (DRT) analysis was conducted during the early stage of CIP polymerization, as shown in Figure 3e. The DRT spectra exhibit three well-resolved relaxation peaks, which can be assigned to the charge-transfer resistance (R_{ct}), the SEI-related interfacial resistance (R_{SEI}), and an additional low-frequency process (R_x) associated with ion transport polarization.[39] Notably, the intensities of all three peaks progressively decrease as the CIP polymerization proceeds, indicating a continuous reduction in the overall interfacial and transport resistances. This simultaneous attenuation suggests that the polymerization process not only improves charge-transfer kinetics but also facilitates Li^+ transport across the SEI and suppresses concentration polarization. These kinetic signatures are fully consistent with the anion-confinement-induced electrolyte reconfiguration, which preserves favorable Li^+ mobility while progressively lowering interfacial impedance. Figure 3f schematically illustrates the fundamentally different Li^+ transport mechanisms in TIP and CIP polymer electrolytes. In the TIP electrolyte, complete polymerization leads to a rigid polymer network that indiscriminately traps both Li^+ and anions, resulting in sluggish ion transport and low t^+. By contrast, the CIP strategy selectively immobilizes PF_6^- derived species through Lewis acid-VC interactions and polymer entrapment, while preserving continuous Li^+ migration pathways along polar polymer segments and residual mobile species.[40−42] Figure 3g shows that the CIP electrolyte uniquely combines high σ with an elevated t^+, surpassing most recently reported polymer electrolytes and breaking the long-standing conductivity−selectivity balance.[7,13,42−54]

2.4. Electrochemical Performance of CIP Electrolytes in LMBs

The improved Li^+ transport kinetics enabled by anion confinement are anticipated to alleviate transport-induced polarization and stabilize interfacial ion flux during battery operation. Accordingly, Figure 4 systematically evaluates whether the anion-confinement-enabled transport advantages of the CIP electrolyte can be translated into device-level performance in LMBs. As shown in Figure 4a, the cyclic voltammetry (CV) profiles of the CIP-based cell exhibit well-

https://doi.org/10.1021/acsami.6c06006
ACS Appl. Mater. Interfaces 2026, 18, 35312−35323

Downloaded from pubs.acs.org/aamick/article-pdf/18/25/35312/6511266/acsami.6c06006.pdf by SOUTHWEST JIAOTONG UNIV user on 07 November 2026

defined redox features with minimal polarization and good overlap over repeated scans, indicating favorable electrochemical reversibility and fast reaction kinetics enabled by the polymer electrolyte. The rate capability of LMBs employing TIP and CIP electrolytes is compared in Figure 4b. Across a wide current density range from 0.1 to 10 C, the CIP-based cell consistently delivers higher reversible capacities, particularly under high-rate conditions, where transport limitations become increasingly dominant. Notably, at 5 and 10 C, the CIP electrolyte maintains a discharge capacity of 87 mAh g^{-1} and 68 mAh g^{-1}, respectively. This performance markedly exceeds that of the TIP counterpart, highlighting the effectiveness of enhanced Li^+ transport kinetics and elevated transference numbers in mitigating concentration polarization. The representative charge/discharge voltage profiles of the CIP-based battery at various C-rates are presented in Figure 4c. Even at high rates up to 10 C, the cell preserves well-defined voltage plateaus with reduced polarization, further confirming the robust ionic transport and interfacial compatibility of the CIP electrolyte.

Long-term cycling performance was subsequently assessed at 0.5 C, as shown in Figure 4d. The CIP-based battery delivers a stable reversible capacity of 126 mAh g^{-1} over 1200 cycles with an average Coulombic efficiency (CE) of 99.98%, whereas the TIP-based cell suffers from pronounced capacity decay and fluctuating efficiency after only 200 cycles. This pronounced difference underscores the critical role of anion confinement and moderated polymerization in sustaining long-term electrochemical stability. To probe the evolution of interfacial resistance, electrochemical impedance spectroscopy (EIS) measurements were conducted before and after prolonged cycling (Figure 4e). The CIP-based cell exhibits only a marginal increase in interfacial resistance after cycling, from 105 Ω cm^{-2} to 241 Ω cm^{-2}, suggesting the formation of a stable and low-resistance electrode/electrolyte interface. The high-rate durability of the CIP electrolyte was further examined under an aggressive current density of 10 C (Figure 4f and S17). Remarkably, the CIP-based battery maintains stable cycling over 2000 cycles with a CE approaching 99.90%, demonstrating exceptional tolerance to high-rate operation and sustained Li^+ flux. Collectively, these electrochemical results demonstrate that the anion-confinement strategy not only enhances bulk ionic transport but also profoundly influences interfacial electrochemical behavior under practical operating conditions.

2.5. Stabilization of the Lithium Metal Anode and SEI Evolution

Figure 5a compares the lithium nucleation overpotential in TIP and CIP electrolytes. The TIP electrolyte exhibits a relatively high nucleation overpotential of 36.9 mV, whereas the CIP electrolyte shows a substantially reduced value (14.2 mV). The markedly lower nucleation overpotential in the CIP system indicates a reduced energy barrier for lithium nucleation, enabling more facile and homogeneous initial Li deposition. This behavior suggests that the anion-confinement-induced interfacial chemistry in the CIP electrolyte promotes uniform Li^+ flux and mitigates localized current density amplification at the electrode surface, thereby laying the foundation for stabilized lithium plating/stripping behavior.[55] Figure 5b and Figure S18 compare the CE evolution of Li−Cu cells using TIP and CIP electrolytes at a current density of 0.2 mA cm^{-2} with an areal capacity of 0.4 mAh cm^{-2}. The TIP electrolyte sustains nearly 100% CE for only ∼15 cycles, followed by a rapid decay, indicative of continuous parasitic reactions and irreversible lithium loss. In contrast, the CIP electrolyte maintains a stable CE of ∼100% for more than 80 cycles, demonstrating markedly improved reversibility of lithium plating/stripping. This extension in CE lifetime highlights the superior compatibility and interfacial stability of the CIP electrolyte toward lithium metal, arising from its regulated interfacial chemistry and suppressed side reactions during repeated cycling.

Figure 5c evaluates the critical current density (CCD) of symmetric Li cells by stepwise increasing the current density from 0.1 to 5 mA cm^{-2}. Across the entire current range, the CIP electrolyte consistently exhibits lower polarization than the TIP counterpart, indicating reduced interfacial resistance and more uniform Li^+ flux at the lithium surface. Notably, the CIP-based cell remains electrochemically stable up to a current density of 3 mA cm^{-2} without signs of short-circuiting, whereas the TIP-based cell fails rapidly at elevated current densities. This pronounced contrast demonstrates that the CIP electrolyte effectively suppresses dendritic lithium growth and accommodates high-rate Li plating/stripping, thereby delivering a substantially higher critical current density and improved tolerance to aggressive operating conditions. In addition, the mechanical robustness of the CIP electrolyte was further evaluated. As shown in Figure S19 and Movies S3−S4, the electrolyte exhibited a Young's modulus of approximately 64 MPa, a tensile strength of 10.16 MPa, and an elongation at break of 263.3%, demonstrating an excellent balance between mechanical robustness and flexibility. This moderate modulus is well-matched to lithium metal, enabling the electrolyte to accommodate interfacial volume fluctuations during repeated Li plating/stripping while providing mechanical resistance against dendrite penetration.

Building upon the enhanced critical current density and mechanical compliance of the CIP electrolyte, its ability to sustain long-term lithium plating/stripping was further evaluated using symmetric Li cells. As shown in Figure 5d, under a current density of 0.5 mA cm^{-2}, the cell employing the TIP electrolyte exhibits rapidly increasing polarization and undergoes pronounced short-circuit failure after approximately 400 h, indicative of unstable lithium deposition and uncontrolled dendritic growth. In contrast, the CIP-based symmetric cell delivers highly stable and flat voltage profiles for over 2000 h without noticeable fluctuation, demonstrating a markedly improved tolerance toward prolonged lithium cycling. The superior interfacial stability afforded by the CIP electrolyte is further corroborated by EIS in Figure 5e; the Nyquist plots collected before and after long-term cycling show only a marginal increase in interfacial resistance for the CIP system, with the total interfacial impedance increasing slightly from 79 Ω cm^{-2} to 154 Ω cm^{-2}. Such minimal impedance evolution evidences the formation of a robust and dynamically stable SEI layer, effectively suppressing continuous side reactions and preserving fast charge transfer kinetics at the lithium metal interface.

To elucidate the morphological origin of the enhanced electrochemical behavior, photographs of lithium metal after cycling are shown in Figure S20. Lithium deposited in the TIP electrolyte exhibits a highly porous and mossy morphology, accompanied by abundant dendritic filaments, indicative of uncontrolled lithium growth and severe interfacial instability. In stark contrast, the lithium surface cycled in the CIP

Downloaded from pubs.acs.org/aamick/article-pdf/18/25/35312/6511266/acsami.6c06006.pdf by SOUTHWEST JIAOTONG UNIV user on 07 November 2026

https://doi.org/10.1021/acsami.6c06006
ACS Appl. Mater. Interfaces 2026, 18, 35312−35323

electrolyte remains dense, smooth, and compact, with no discernible dendritic features, demonstrating the effective regulation of lithium deposition and providing a direct morphological explanation for the prolonged cycling stability and delayed short-circuit behavior observed in symmetric cells. Further insight into the chemical nature of the stabilized interface was obtained from X-ray photoelectron spectroscopy (XPS). Figure 5f compares the F 1s spectra of the CIP electrolyte before and after prolonged cycling. After cycling, a pronounced peak centered at approximately 685 eV emerged, which is characteristic of LiF formation. The enrichment of LiF indicates the construction of an inorganic-rich SEI layer, which is widely recognized for its high mechanical robustness and favorable Li^+ transport capability. Such a LiF-dominated SEI effectively passivates the lithium surface, suppresses continuous electrolyte decomposition, and homogenizes the interfacial ion flux, thereby mitigating dendritic growth.

Integrating the electrochemical, morphological, and spectroscopic evidence, Figure 5g schematically illustrates the distinct interfacial evolution pathways enabled by the two electrolytes. In the TIP system, uncontrolled solvent decomposition and nonuniform ion transport give rise to a fragile, organic-rich SEI, leading to localized current hotspots, accelerated dendrite formation, and rapid cell failure. In contrast, the CIP electrolyte induces a regulated interfacial reaction sequence, favoring early-stage $LiPF_6$-derived inorganic species formation and the development of a compact, LiF-rich SEI.[56] This reconstructed interface ensures uniform Li^+ flux, suppresses dendritic lithium growth, and underpins the exceptional long-term cycling stability of the LMBs.

3. CONCLUSION

This work establishes an ambient cationic activation-radical synergy strategy that fundamentally redefines the role of PF_6^- anions in polymer electrolyte chemistry. Distinct from conventional thermal radical polymerization, PF_6^- derived Lewis acidic species are selectively activated and kinetically trapped by AIBN and VC monomers, initiating room-temperature polymerization through a cationic-induced pathway that precedes and catalytically couples with radical propagation. This regulated reaction sequence enables controlled polymer growth while preserving a fraction of mobile monomers and lithium salts, thereby avoiding the complete ion immobilization that typically plagues in situ polymerized electrolytes. As a result, the reconstructed electrolyte chemistry enforces progressive anion confinement while maintaining Li^+ as the dominant mobile charge carrier, delivering accelerated ion transport kinetics with an ionic conductivity of 6.49×10^{-3} S cm^{-1} and an elevated Li^+ transference number of 0.78. When applied in LMBs, this electrolyte promotes the formation of a dense, inorganic-rich, and dynamically reinforced SEI, leading to homogeneous lithium deposition, reduced nucleation overpotential of 14.2 mV, stable Li−Li cycling for over 2000 h at 0.5 mA cm^{-2}, and long-term LMB operation exceeding 1200 cycles at 0.5 C. Beyond performance metrics, this study reveals a direct mechanistic linkage between anion-involved polymerization chemistry, ion-transport hierarchy, and interfacial reaction priority, offering a chemically intuitive and generalizable design paradigm for next-generation high-performance LMBs.

4. EXPERIMENTAL SECTION

4.1. Materials

Lithium hexafluorophosphate ($LiPF_6$) was obtained from Tokyo Chemical Industry (TCI, Japan). Vinylene carbonate (VC) and azobis(isobutyronitrile) (AIBN) were purchased from Aladdin Reagent Co., Ltd. Lithium metal foils (250 μm thick) were supplied by China Energy Lithium Co., Ltd. Lithium iron phosphate ($LiFePO_4$, LFP) cathodes with a nominal specific capacity of 160 mAh g^{-1} were purchased from MTI Corporation. All materials were used as received unless otherwise specified. All procedures involving moisture-sensitive materials were carried out in an argon-filled glovebox with H_2O and O_2 levels maintained below 0.1 ppm.

4.2. Electrolyte Preparation

The traditional thermal-initiated polymerization (TIP) electrolyte was prepared by dissolving 1.52 g of $LiPF_6$ in 1 mL of VC containing 2 mg of AIBN as the radical initiator. The resulting solution was sealed and thermally polymerized in an oven at 60 °C for 6 h. For the cationic-activated pathway (CIP) electrolyte, the same precursor solution was transferred into an argon-filled glovebox and allowed to polymerize at ambient temperature for 24 h without external heating. Unless otherwise noted, all electrolyte preparation procedures were conducted under an inert argon atmosphere.

4.3. Materials Characterization

The morphology and microstructure of the as-prepared TIP and CIP electrolytes were examined using a field-emission scanning electron microscope (SEM, JEOL JSM-7800F) operated at 5 kV. Crystal structures were analyzed by X-ray diffraction (XRD, PANalytical). Fourier transform infrared (FT-IR) spectra were collected on a Bruker Invenio spectrometer. Nuclear magnetic resonance (NMR) spectra, including ^1H, ^{13}C, ^{19}F, and ^{31}P, were recorded on a JEOL JNM-ECA600 spectrometer using deuterated dimethyl sulfoxide (DMSO-d_6) as the solvent. X-ray photoelectron spectroscopy (XPS) measurements were conducted on a Thermo Scientific K-Alpha system with Al Kα radiation to evaluate the surface chemical composition of cycled lithium metal. Tensile strength was carried out on an LDW1 Tensile Tester (100 N Load Cell).

4.4. Electrochemical Performance Characterization

The ionic conductivities (σ, S·cm^{-1}) of the polymer electrolyte were measured by electrochemical impedance spectroscopy (EIS) on a CHI660E electrochemical workstation over a frequency range of 0.1 Hz to 1 MHz. The electrolyte membrane was sandwiched between two stainless-steel (SS) blocking electrodes (16 mm) and sealed in a coin cell. The ionic conductivity was calculated according to eq 1.

$$\sigma = \frac{L}{R \cdot S} \tag{1}$$

where L (cm) represents the thickness of the membrane, R (Ω) represents the resistance value of the bulk electrolyte acquired from EIS, and S (cm^2) represents the area of the stainless steel.

The electrochemical stability window of the solid-state electrolytes (SSEs) was evaluated using asymmetric SS/electrolyte/Li cells via linear sweep voltammetry (LSV) from the open-circuit voltage (OCV) to 6.0 V (vs Li^+/Li).

The lithium-ion transference number (t_{Li^+}) was measured by a combination measurement of AC impedance and DC polarization in a symmetric Li/electrolyte/Li cell. The value of t_{Li^+} can be calculated by the following (eq 2):

$$t_{Li^+} = \frac{I_s(\Delta V - I_0 R_s)}{I_0(\Delta V - I_S R_0)} \tag{2}$$

where ΔV represents the applied polarization potential (10 mV), I_0 and I_s represent the initial current and steady current obtained by the polarization curve, and R_0 and R_s represent the interfacial resistances before and after polarization.

CR2032-type coin cells were assembled using a $LiFePO_4$ (LFP) cathode with an areal capacity of 1.7 mAh cm^{-2} a 250 μm lithium

Downloaded from pubs.acs.org/aamick/article-pdf/18/25/35312/6511266/acsami.6c06006.pdf by SOUTHWEST JIAOTONG UNIV user on 07 November 2026

https://doi.org/10.1021/acsami.6c06006
ACS Appl. Mater. Interfaces 2026, 18, 35312−35323

metal anode, and TIP or CIP polymer electrolytes. Rate capability tests were performed from 0.1 to 10 C within a voltage window of 2.5−4.0 V (1 C = 170 mA g^{-1}) on a Neware CT4008 multichannel battery tester.

4.5. DFT Calculation

Density functional theory (DFT) calculations were performed to elucidate the decomposition behavior of PF_6^-, the activation mechanism of AIBN and VC, and the associated interfacial reaction pathways. All calculations were conducted using the DMol^3 package within the Materials Studio software. The generalized gradient approximation (GGA) with the Perdew−Burke−Ernzerhof (PBE) functional was employed to describe the exchange-correlation interactions. A double numerical basis set with polarization functions (DNP) was selected to ensure high computational accuracy. Core electrons were treated using the DFT semicore pseudopotential (DSPP). Geometry optimizations were carried out without symmetry constraints until the convergence criteria were satisfied, with the energy tolerance set to 1.0×10^{-5} Ha, the maximum force below 0.002 Ha $Å^{-1}$, and the maximum displacement within 0.005 Å. A conductor-like screening model (COSMO) was applied to account for solvent effects. Transition-state searches were performed using the linear synchronous transit/quadratic synchronous transit (LST/QST) method, followed by frequency analysis to confirm a single imaginary frequency. Reaction energy barriers were determined from the energy difference between the transition state and the corresponding initial state. Adsorption energies were calculated according to:

$$E_{ads} = E_{total} - E_{surface} - E_{species} \quad (3)$$

where E_{total}represents the total energy of the adsorption system, $E_{surface}$ is the energy of the substrate, and $E_{species}$ is the energy of the isolated molecule or ion.

■ ASSOCIATED CONTENT

Supporting Information

The Supporting Information is available free of charge at https://pubs.acs.org/doi/10.1021/acsami.6c06006.

Video recordings showing the room-temperature polymerization process and in situ electrolyte formation (MP4)

Videos demonstrating the effect of BHT addition on AIBN-triggered VC polymerization in VC/$LiPF_6$/AIBN systems (MP4)

Video recording of the impact test of the polymer electrolyte film (MP4)

Video recording of the tensile deformation test of the polymer electrolyte film (MP4)

Additional experimental details and characterization data, including ^{1}H and ^{13}C NMR spectra of VC monomer and polymer electrolytes; XPS analyses of polymerized electrolytes; photographs documenting room-temperature polymerization behavior, lithium-salt effects, gelation evolution, and in situ electrolyte formation; SEM images of surface and cross-sectional morphologies; XRD patterns and thermogravimetric analysis (TGA) of polymer electrolytes; electrochemical characterization, including ionic conductivity, Li^+ transference number measurements, electrochemical stability window evaluation, and Li||Cu cell performance; mechanical properties; and postcycling lithium metal anode morphology observations (PDF)

■ AUTHOR INFORMATION

Corresponding Author

Weiqing Yang − *Key Laboratory of Advanced Technologies of Materials (Ministry of Education), School of Materials Science and Engineering, Southwest Jiaotong University, Chengdu 610031, China; Research Institute of Frontier Science, Southwest Jiaotong University, Chengdu 610031, China;* orcid.org/0000-0001-8828-9862; Email: wqyang@swjtu.edu.cn

Authors

Zhong Xu − *Key Laboratory of Advanced Technologies of Materials (Ministry of Education), School of Materials Science and Engineering, Southwest Jiaotong University, Chengdu 610031, China; Yibin Research Institute of Southwest Jiaotong University, Yibing 644000, China; Research Institute of Frontier Science, Southwest Jiaotong University, Chengdu 610031, China;* orcid.org/0009-0003-0900-8543

Weili Deng − *Key Laboratory of Advanced Technologies of Materials (Ministry of Education), School of Materials Science and Engineering, Southwest Jiaotong University, Chengdu 610031, China;* orcid.org/0000-0003-1427-534X

Complete contact information is available at: https://pubs.acs.org/10.1021/acsami.6c06006

Notes

The authors declare no competing financial interest.

■ ACKNOWLEDGMENTS

This work was supported by the National Science Foundation of China (No. 52372228), the Yibin Science and Technology Innovation Seeding Project (No. 2025MZ009), and the Fundamental Research Funds for the Central Universities (No. 2682026CX250). The authors thank the help from the Analysis and Testing Center of Southwest Jiaotong University and Ceshigo for testing (www.ceshigo.com).

■ REFERENCES

(1) Zhang, W.; et al. Single-phase local-high-concentration solid polymer electrolytes for lithium-metal batteries. *Nature Energy* **2024**, *9*, 386−400.

(2) Zou, S.; et al. In situ polymerization of solid-state polymer electrolytes for lithium metal batteries: a review. *Energy Environ. Sci.* **2024**, *17*, 4426−4460.

(3) Peng, H.; et al. Molecular Design for In-Situ Polymerized Solid Polymer Electrolytes Enabling Stable Cycling of Lithium Metal Batteries. *Adv. Energy Mater.* **2024**, *14*, 2400428.

(4) Sand, S. C.; Rupp, J. L. M.; Yildiz, B. A critical review on Li-ion transport, chemistry and structure of ceramic−polymer composite electrolytes for solid state batteries. *Chem. Soc. Rev.* **2025**, *54*, 178−200.

(5) Lu, C.; et al. High-performance fibre battery with polymer gel electrolyte. *Nature* **2024**, *629*, 86−91.

(6) Lu, P.; et al. Materials and chemistry design for low-temperature all-solid-state batteries. *Joule* **2024**, *8*, 635−657.

(7) Zhang, S.; et al. Moderate Li ± solvent binding for gel polymer electrolytes with stable cycling toward lithium metal batteries. *Energy Environ. Sci.* **2025**, *18*, 3807−3816.

(8) Ren, Y.; et al. Mixing Functionality in Polymer Electrolytes: A New Horizon for Achieving High-Performance All-Solid-State Lithium Metal Batteries. *Angew. Chem. Int. Ed.* **2025**, *64*, No. e202422169.

Downloaded from pubs.acs.org/aamick/article-pdf/18/25/35312/6511266/acsami.6c06006.pdf by SOUTHWEST JIAOTONG UNIV user on 07 November 2026

(9) Bai, M.; et al. An in-situ polymerization strategy for gel polymer electrolyte Si||Ni-rich lithium-ion batteries. *Nat. Commun.* **2024**, *15*, 5375.
(10) Yang, S.-J.; et al. Intrinsically Safe Lithium Metal Batteries Enabled by Thermo-Electrochemical Compatible In Situ Polymerized Solid-State Electrolytes. *Adv. Mater.* **2024**, *36*, 2405086.
(11) Li, D.; et al. High Ionic Conductive, Mechanical Robust Sulfide Solid Electrolyte Films and Interface Design for All-Solid-State Lithium Metal Batteries. *Adv. Funct. Mater.* **2024**, *34*, 2315555.
(12) Chen, X.; et al. Contriving a gel polymer electrolyte to drive quasi-solid-state high-voltage Li metal batteries at ultralow temperatures. *Energy Environ. Sci.* **2025**, *18*, 910−922.
(13) Chai, J.; et al. In Situ Generation of Poly (Vinylene Carbonate) Based Solid Electrolyte with Interfacial Stability for LiCoO2 Lithium Batteries. *Adv. Sci.* **2017**, *4*, 1600377.
(14) Du, Y.; et al. Ameliorating structural and electrochemical properties of traditional poly-dioxolane electrolytes via integrated design of ultra-stable network for solid-state batteries. *Energy Storage Mater.* **2023**, *56*, 310−318.
(15) Mu, K.; et al. Hybrid Crosslinked Solid Polymer Electrolyte via In-Situ Solidification Enables High-Performance Solid-State Lithium Metal Batteries. *Adv. Mater.* **2023**, *35*, 2304686.
(16) Xu, H.; et al. In Situ Topological Interphases Boosting Stable Solid-State Lithium Metal Batteries. *Adv. Energy Mater.* **2023**, *13*, 2204411.
(17) Spotte-Smith, E. W. C.; Petrocelli, T. B.; Patel, H. D.; Blau, S. M.; Persson, K. A. Elementary Decomposition Mechanisms of Lithium Hexafluorophosphate in Battery Electrolytes and Interphases. *ACS Energy Lett.* **2023**, *8*, 347−355.
(18) Buitrago Botero, P. J.; Ells, A. W.; Svirinovsky-Arbeli, A.; Juelsholt, M.; Marbella, L. E. Counterion Lewis Acidity Determines the Rate of Hexafluorophosphate Hydrolysis in Nonaqueous Battery Electrolytes. *J. Am. Chem. Soc.* **2025**, *147*, 9159−9174.
(19) Jiang, H.; et al. A PF6−-Permselective Polymer Electrolyte with Anion Solvation Regulation Enabling Long-Cycle Dual-Ion Battery. *Adv. Mater.* **2022**, *34*, 2108665.
(20) Meng, Y.; et al. Synergistic Lewis Acid and Hydrogen Bonding Strategy to Enable Polymerized and Wide-Temperature Li-Fe-F Conversion Solid-State Batteries. *Adv. Energy Mater.* **2025**, *15*, No. e02645.
(21) Savoie, B. M.; Webb, M. A.; Miller, T. F., III. Enhancing Cation Diffusion and Suppressing Anion Diffusion via Lewis-Acidic Polymer Electrolytes. *J. Phys. Chem. Lett.* **2017**, *8*, 641−646.
(22) Liu, F. Q.; et al. Upgrading traditional liquid electrolyte via in situ gelation for future lithium metal batteries. *Sci. Adv.* **2018**, *4*, No. eaat5383.
(23) Dong, T.; et al. A rigid-flexible coupling poly(vinylene carbonate) based cross-linked network: A versatile polymer platform for solid-state polymer lithium batteries. *Energy Storage Mater.* **2022**, *50*, 525−532.
(24) Zhu, K.; Yang, J.; Li, Y.; Xu, T.; Pan, Q. Self-Adaptive Poly(Vinylene Carbonate) Based Electrolytes for Zero-Pressure and High-Temperature Solid-State Lithium Metal Batteries. *Adv. Funct. Mater.* **2026**, *36*, No. e24843.
(25) Kwon, H.; et al. Weakly coordinated Li ion in single-ion-conductor-based composite enabling low electrolyte content Li-metal batteries. *Nat. Commun.* **2023**, *14*, 4047.
(26) Chen, Z.; et al. High-energy lithium batteries based on single-ion conducting polymer electrolytes and Li[Ni0.8Co0.1Mn0.1]O2 cathodes. *Nano Energy* **2020**, *77*, 105129.
(27) Kamigaito, M.; Sawamoto, M. Synergistic Advances in Living Cationic and Radical Polymerizations. *Macromolecules* **2020**, *53*, 6749−6753.
(28) He, H.; et al. Insight into the Tuning Fluorination of Carbonates for Lithium-Ion Batteries: A Theoretical Study. *J. Phys. Chem. B* **2025**, *129*, 7248−7269.
(29) Xu, K. Nonaqueous Liquid Electrolytes for Lithium-Based Rechargeable Batteries. *Chem. Rev.* **2004**, *104*, 4303−4418.
(30) Chen, Y.; Gao, S.; Su, Y.; Chen, T.; Fu, J. Multiscale Design Strategies of Interface-Stabilized Solid Electrolytes and Dynamic Interphase Decoding from Atomic-to-Macroscopic Perspectives. *Adv. Energy Mater.* **2025**, *15*, No. e02938.
(31) Wu, Q.; et al. Phase regulation enabling dense polymer-based composite electrolytes for solid-state lithium metal batteries. *Nat. Commun.* **2023**, *14*, 6296.
(32) Pei, F.; et al. Interfacial self-healing polymer electrolytes for long-cycle solid-state lithium-sulfur batteries. *Nat. Commun.* **2024**, *15*, 351.
(33) Jiang, F.-N.; et al. Thermoresponsive Electrolytes for Safe Lithium-Metal Batteries. *Adv. Mater.* **2023**, *35*, 2209114.
(34) Allen, J. P.; et al. Transition metal coordination to degradation products in battery electrolytes revealed by NMR and EPR spectroscopy. *Energy Environ. Sci.* **2025**, *18*, 10147−10163.
(35) Han, J.-G.; Kim, K.; Lee, Y.; Choi, N.-S. Scavenging Materials to Stabilize LiPF6-Containing Carbonate-Based Electrolytes for Li-Ion Batteries. *Adv. Mater.* **2019**, *31*, 1804822.
(36) Zhang, S.; et al. A family of oxychloride amorphous solid electrolytes for long-cycling all-solid-state lithium batteries. *Nat. Commun.* **2023**, *14*, 3780.
(37) Li, W.-Y.; et al. Cation Vacancy-Boosted Lewis Acid−Base Interactions in a Polymer Electrolyte for High-Performance Lithium Metal Batteries. *ACS Appl. Mater. Interfaces* **2021**, *13*, 51107−51116.
(38) Wang, M.; et al. Fluoroethylene Carbonate-Enabled Gel Polymer Electrolyte for Stable High-Voltage Lithium Metal Batteries. *Adv. Mater.* **2025**, *37*, 2502076.
(39) Lu, Y.; Zhao, C.-Z.; Huang, J.-Q.; Zhang, Q. The timescale identification decoupling complicated kinetic processes in lithium batteries. *Joule* **2022**, *6*, 1172−1198.
(40) Xu, R.; et al. Polymer-Modulated Solvation Chemistry via Compatibilizing-Solvent Plasticization for Stable High-Energy Lithium Metal Batteries. *J. Am. Chem. Soc.* **2026**.
(41) Zhu, G.-R.; et al. Non-flammable solvent-free liquid polymer electrolyte for lithium metal batteries. *Nat. Commun.* **2023**, *14*, 4617.
(42) Lu, Y.; et al. Toward practical lithium metal batteries via a solvation structure regulation strategy in in situ polymerized fluorinated gel polymer electrolytes. *Energy Environ. Sci.* **2025**, *18*, 9512−9523.
(43) Neumann, P.; et al. Design of an Amphiphilic Anion toward High Loading Solid-State Lithium Metal Battery. *Small* **2026**, *22*, No. e07567.
(44) Li, T.; et al. Li7La3Zr2O12/Polymethacrylate-Based Composite Electrolyte with Hybrid Solid Electrolyte Interphase for Ultra-stable Solid-State Lithium Batteries. *Nano Micro Lett.* **2026**, *18*, 189.
(45) Shah, V.; Utomo, N. W.; Sinha, R.; Gao, X.; Wang, Y.; Gao, Z.; Singh, S.; Archer, L. A.; Joo, Y. L.; et al. In-Situ Gelled Hybrid Polymer-Ceramic Electrolytes: Empowering Superior Performance and Stability in Lithium-Sulfur Batteries. *Adv. Energy Mater.* **2026**, *16*, No. e05041.
(46) Liu, S.; et al. Bioinspired gel polymer electrolyte for wide temperature lithium metal battery. *Nat. Commun.* **2025**, *16*, 2474.
(47) Chen, J.; et al. Tri-functional molecular motif-engineered polymer electrolytes for high-voltage lithium metal batteries. *Energy Storage Mater.* **2026**, *84*, 104835.
(48) Hong, Y. K.; et al. Intermolecular Hydrogen-Bond Network Boosts Lithium-Bonding Kinetics in Solid-State Lithium Metal Batteries. *ACS Nano* **2026**, *20*, 1665−1677.
(49) Gou, J.; et al. An anisotropic strategy for developing polymer electrolytes endowing lithium metal batteries with electrochemo-mechanically stable interface. *Nat. Commun.* **2025**, *16*, 3626.
(50) Fu, H.; Chen, Z.; Xu, Y.; Ye, X.; Zhong, Y.; Wang, X.; Tu, J.; et al. Fluorinated Segmental Dilution Constructs Low-Temperature Tolerant Localized High-Concentration Polymer Electrolytes for Lithium Metal Batteries. *Adv. Funct. Mater.* **2026**, *36*, No. e29863.
(51) Nie, L.; et al. Regulating ion transport and solvation chemistry in zwitterionic gel polymer electrolyte for high-performance quasi-solid-state batteries. *Proc. Natl. Acad. Sci. U. S. A.* **2026**, *123*, No. e2513940123.

Downloaded from pubs.acs.org/aamick/article-pdf/18/25/35312/6511266/acsami.6c06006.pdf by SOUTHWEST JIAOTONG UNIV user on 07 November 2026

(52) Li, Z.; et al. "Gene-Editing" Design Upgrades Eutectic-Polymer Electrolytes with Ultra-High Li+ Conductivity. *Angew. Chem. Int. Ed.* **2025**, *64*, No. e202508857.
(53) Liu, X.; et al. Carbon Dots Induced Supramolecular Gel Polymer Electrolyte for High-Performance Lithium Metal Batteries. *Adv. Energy Mater.* **2025**, *15*, 2405433.
(54) Chen, Y.; et al. A Gradient Nanodomain High-Entropy Polymer Electrolyte Tape for Pressure-Free Solid-State Lithium Batteries. *Adv. Mater.* **2026**, *38*, No. e20657.
(55) Chen, Y.; et al. Electron-funnel mediated anion confinement enables ultra-reversible interphases in solid-state batteries. *eScience* **2026**, *6*, 100452.
(56) Wagner-Henke, J.; Kuai, D.; Balbuena, P. B.; Krewer, U. Understanding the effect of vinylene carbonate on SEI formation, morphology and stability on lithium metal anodes. *Energy Storage Mater.* **2025**, *81*, 104434.

Downloaded from pubs.acs.org/aamick/article-pdf/18/25/35312/6511268/acsami.6c06006.pdf by SOUTHWEST JIAOTONG UNIV user on 07 November 2026

https://doi.org/10.1021/acsami.6c06006
ACS Appl. Mater. Interfaces 2026, 18, 35312−35323